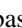






Decreasing ultrafast x-ray pulse durations with saturable absorption and resonant transitionsSebastian Cardoch ^{1,*} Fabian Trost ² Howard A. Scott ³ Henry N. Chapman ^{2,4,5}
Carl Caleman,^{1,2} and Nicusor Timneanu ^{1,†}¹*Department of Physics and Astronomy, Uppsala University, Box 516, SE-751 20 Uppsala, Sweden*²*Center for Free-Electron Laser Science CFEL, Deutsches-Elektronen Synchrotron DESY, Notkestr. 85, 22607 Hamburg, Germany*³*Lawrence Livermore National Laboratory, L-18, P.O. Box 808, Livermore, California 94550, USA*⁴*The Hamburg Center for Ultrafast Imaging, Universität Hamburg, Luruper Chaussee 149, 22761 Hamburg, Germany*⁵*Department of Physics, Universität Hamburg, Luruper Chaussee 149, 22761 Hamburg, Germany*

(Received 12 October 2022; accepted 9 December 2022; published 17 January 2023)

Saturable absorption is a nonlinear effect where a material's ability to absorb light is frustrated due to a high influx of photons and the creation of electron vacancies. Experimentally induced saturable absorption in copper revealed a reduction in the temporal duration of transmitted x-ray laser pulses, but a detailed account of changes in opacity and emergence of resonances is still missing. In this computational work, we employ nonlocal thermodynamic equilibrium plasma simulations to study the interaction of femtosecond x rays and copper. Following the onset of frustrated absorption, we find that a K - M resonant transition occurring at highly charged states turns copper opaque again. The changes in absorption generate a transient transparent window responsible for the shortened transmission signal. We also propose using fluorescence induced by the incident beam as an alternative source to achieve shorter x-ray pulses. Intense femtosecond x rays are valuable to probe the structure and dynamics of biological samples or to reach extreme states of matter. Shortened pulses could be relevant for emerging imaging techniques.

DOI: [10.1103/PhysRevE.107.015205](https://doi.org/10.1103/PhysRevE.107.015205)**I. INTRODUCTION**

X-ray free-electron lasers (XFELs) can generate pulses with unprecedented characteristics suitable to study the structure and dynamics of biological samples [1], ultrafast phase transitions [2], or exotic states of matter [3]. A current goal is to produce high-intensity (10^{17} – 10^{19} W/cm²) extremely short pulses of tens of femtosecond that can image matter at ångström resolution before the onset of radiation damage or atomic motion [4,5]. Recent suggestions for a new technique, incoherent diffractive imaging [6], require the development of x-ray pulses shorter than the coherence time of fluorescence emission [7]. The intense pulses from XFELs can alter the structure and optical properties of materials, resulting in nonlinear effects. Taking advantage of this material response, Inoue *et al.* [8] experimentally demonstrated temporal shortening of x rays by inducing saturable absorption in a solid copper target, thus uncovering a potential approach to satisfy the pulse constraints for incoherent imaging.

Saturable absorption, which describes fluence-induced transparency, has been investigated in the soft and hard x-ray

regimes on transition metals such as aluminum [9,10] and iron [11]. The initially opaque target attenuates the incoming radiation until depletion of electrons in the K shell weakens the interactions of photons with core electrons, and the sample achieves a transparent state if the photoionization rate is comparable to the Auger-Meitner and fluorescence decay rates [12]. The electronic vacancies that emerge kickstart a series of intermediate steps that cause broadening and shifting of the K edge to higher energies, also contributing to changes in opacity. Inoue *et al.* [8] measured the transmission of x rays through copper and found a detectable temporal decrease compared to the incident beam at a few selected fluences. The study opened interesting questions about the dynamic processes inside the material and how the level of ionization and electronic rearrangement governs the transmission.

In this paper, we computationally investigate why XFEL beams transmitted through copper have shorter temporal durations. We also explore Cu fluorescence, induced by absorption of the incident beam, as an alternative source of x rays that might exhibit reduced temporal characteristics. We chose a copper target to contrast and validate our calculations with the results of the experiment performed by Inoue *et al.* [8]. Copper has comparable fluorescence and Auger-Meitner electron yields with its $K\alpha$ emission found above iron's, cobalt's, and nickel's K edge. Transmission or fluorescence originating from the copper target can generate core vacancies on these lower Z elements, found in crystals or biomolecules, whose fluorescence could be applied for structure determination [6].

High-intensity x rays with wavelengths just above copper's K -edge experience significant absorption in the material

*sebastian.cardoch@physics.uu.se

†nicusor.timneanu@physics.uu.se

Published by the American Physical Society under the terms of the [Creative Commons Attribution 4.0 International](https://creativecommons.org/licenses/by/4.0/) license. Further distribution of this work must maintain attribution to the author(s) and the published article's title, journal citation, and DOI. Funded by [Bibsam](https://www.bibsam.de/).

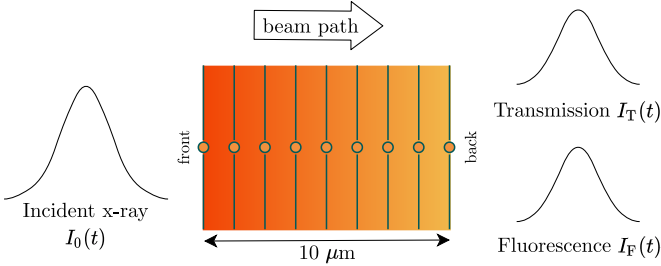


FIG. 1. Schematic representation of a 1D simulation that follows the effects of an incident Gaussian pulse $I_0(t)$ in the material and monitors transmission $I_T(t)$ and fluorescence $I_F(t)$ intensities. Electron and ion temperatures, radiation landscape, and electronic state are sampled at nine different nodes. The transmission and fluorescence spectra were taken from the back node along the forward direction over a 2π solid angle.

(absorption coefficient 10^3 cm^{-1}). Large quantities of energy are deposited mainly from $1s$ electron ionization leading to further damage to the electronic structure, and the sample becomes a plasma within femtoseconds after exposure [13]. Photon-matter collisions create a cascade of secondary processes and a dynamic radiation energy landscape that results in notable temperature differences between ions and electrons and between the front (facing the beam) and back of the sample [14]. Thermalization and cooling through expansion occur on much longer timescales (1–10 ps), so the material exists in a transient warm-dense-matter state that can be studied by nonlocal thermodynamic equilibrium (NLTE) theory [15–19].

We carried out NLTE simulations with a collisional-radiative model to study a $10\text{-}\mu\text{m}$ -thick copper sample that is illuminated by x rays. We chose a range of fluences (5×10^3 – $7 \times 10^5 \text{ J/cm}^2$) that are relevant in experimental settings of present-day XFELs. The incident beam’s time profile $I_0(t)$ was defined as a Gaussian function with 7 fs full width at half maximum (FWHM), centered at 30 fs, with a 9 keV photon energy, and $\Delta E/E = 1 \times 10^{-3}$ bandwidth [20]. Using a screened hydrogenic model, the material was described by a set of energy levels and transition rates for radiative, collisional, autoionization, and electron capture events. Based on the setup shown in Fig. 1, we computed the transmission time profile $I_T(t)$, fluorescence time profile $I_F(t)$, absorption, and occupations resulting from the photoinduced electronic fluctuations. In an experiment, we expect a delay in the radiation path along the thickness of the material that follows the speed of light (~ 30 fs for $10 \mu\text{m}$). In the simulations, radiation is applied instantaneously at each simulation time step with a magnitude that reflects the material’s current optical properties along the radiation path.

II. RESULTS AND DISCUSSION

A. X-ray transmission and fluorescence

We initially calculated the duration (FWHM) of the intensity profiles $I_T(t)$ and $I_F(t)$ as a function of incident fluence. The intensity at any node (sampling planes) consists of radiation from two origins: transmission of the x-ray beam and emission from the material. These two contributions angle-averaged along the forward direction made up the detected

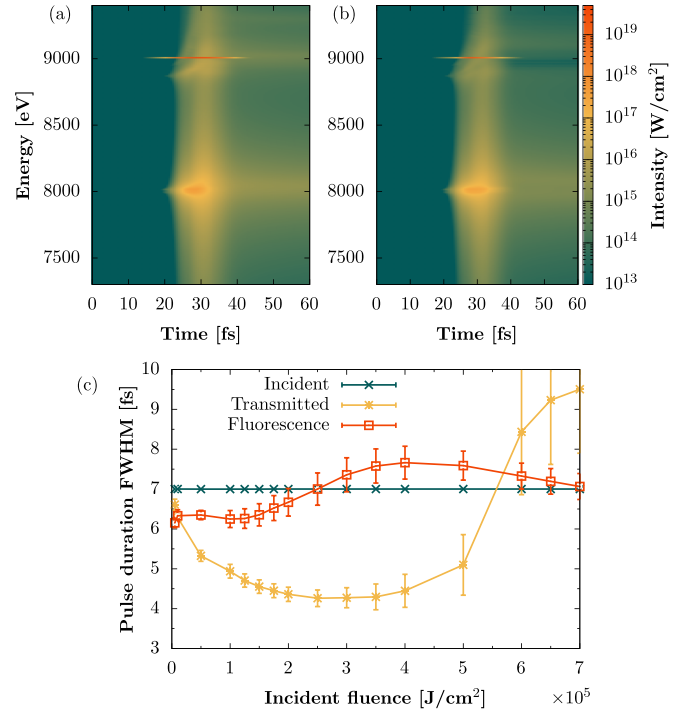


FIG. 2. Calculated intensity at the (a) front and (b) back of the copper slab irradiated with a $3.5 \times 10^5 \text{ J/cm}^2$ pulse. We did not consider a specific detector distance and neglected intensity decays following the inverse square law. $K\alpha_1 = 8012 \text{ eV}$, $K\alpha_2 = 7992 \text{ eV}$, and $K\beta_1 = 8868 \text{ eV}$. (c) Incident, transmitted (9000 eV), and fluorescent (8006 eV) pulse durations with increasing fluence. Error bars represent a 95% confidence bound of the best fit’s width.

intensity spectra that, for a single fluence, are shown in Fig. 2. Panels (a) and (b) correspond to the front and back nodes of the sample, respectively. We used these spectra with varying incident fluences to evaluate the FWHM of the intensity profiles. We defined the fluorescence as the signal that yielded the shortest FWHM and highest peak intensity over the photon energy range between 7 and 9 keV. We divided the spectra in bins of 9 eV [identical to the $I_0(t)$ bandwidth], computed the aspect ratio as peak intensity divided by duration, and found 8006 eV to be the strongest. See the Supplemental Material [21] for details.

We employed a single Gaussian best fit to determine the FWHM and summarized the results in Fig. 2(c). We compared the simulated transmission durations with experimental results shown in Fig. 3(b) from Inoue *et al.* [8]. Our simulations captured a minimum FWHM of 4–5 fs at fluences between 2.5 and $3.5 \times 10^5 \text{ J/cm}^2$, in close agreement with experiments. We observed some discrepancies at low fluences, where experiments showed pulse times longer or similar to the incident beam. Our simulations in contrast returned shorter pulse times than the incident beam. At fluences greater than $3.5 \times 10^5 \text{ J/cm}^2$, the transmission durations increased and, at even higher fluences between 6 and $7 \times 10^5 \text{ J/cm}^2$, the simulations predicted longer durations than the incident x rays. The transmission in these cases featured a double peak that was not well captured by a single Gaussian best fit, resulting in large uncertainty in the FWHM. In the low fluence limit, the final

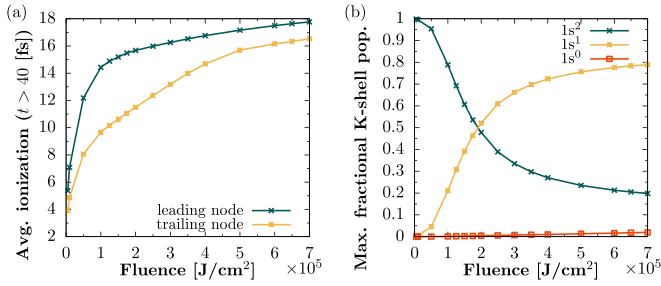


FIG. 3. (a) Average ion charge at the end of the pulse and (b) maximum K -shell population created in the material. The incident photon energy is not large enough to create a second core hole state. We attribute the nonzero $1s^0$ state population to electron-ion collisional ionization. If the rate of this process is faster than the relaxation time of photoionization, a single core hole state can become doubly ionized.

average charge in the copper atoms was below +8, and the generation of core holes was less than 10%, as shown in Fig. 3. The screened hydrogenic model reliably describes a system with significant ionization but loses accuracy for closed-shell and neutral atoms [22]. These artifacts can be corrected by scaling energies to match more detailed calculations [22], but we expect a less accurate system representation in the low ionization regime. The simulations also revealed marginally shorter fluorescence profile FWHM at fluences below $2.0 \times 10^5 \text{ J/cm}^2$.

B. Temporal suppression mechanism

To understand the calculated $I_T(t)$ and $I_F(t)$ intensity profiles with a 9 keV incident beam, we explored the dynamics of the transmission and fluorescence relative to the initial pulse. Figure 4(a) shows normalized profiles for a single fluence of $3.5 \times 10^5 \text{ J/cm}^2$. We found transmission peaked and died out earlier than the incident signal, while the fluorescence persisted over the entire duration of the incident signal. Figures 4(b) and 4(c) generalize these results, displaying $I_T(t)$ and $I_F(t)$ for varying fluences. For transmission, transparency and termination tended to happen at earlier times as fluence increased. Fluorescence FWHM increased with increasing fluence and peak times shifted earlier in time at fluences below $3.5 \times 10^5 \text{ J/cm}^2$ and shifted to later times at higher fluences. Peak times for all three profiles are summarized in Fig. 4(d).

a. Transmission profile. We found saturable absorption offered an incomplete description of transmission profiles. When absorption saturates, the transmitted x rays should match the incident pulse. Instead, our calculations revealed transmission terminated well before the incident beam. Figures 5(a)–5(c) display the absorption coefficient of the material near copper’s K edge as a function of time for fluences of 1.5, 3.5, and $7 \times 10^5 \text{ J/cm}^2$, respectively. In all cases, we observed shifts in the edge plus an opaque feature at photon energies below the edge corresponding to a K – M transition. We found the most dominant contribution to this feature at 9 keV came from a $1s$ – $3p$ transition, where the Cu atoms reached ionization levels between +9 and +17. Increased x-ray absorption with fluence, or so called reverse saturable absorption, due to resonances in the material in the

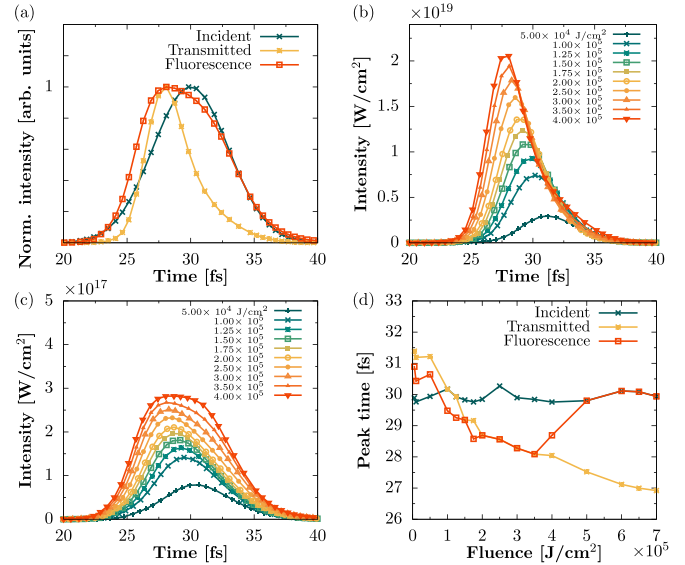


FIG. 4. (a) Radiation dynamics for a $3.5 \times 10^5 \text{ J/cm}^2$ incident beam revealed transmission occurred early in the radiation exposure and extinguished before the peak of the incident pulse at 30 fs. (b) Transmission profiles shifted earlier in time with increasing fluence and (c) emission at 8006 eV became wider with increasing fluence. (d) Summary of peak intensity times. The small variations in the order of subfemtoseconds are due to a combination of the dynamic time step and finite temporal resolution of the simulations.

hard x-ray regime have been reported in the literature [23]. We found at low fluences the shortening of the transmission profile duration was uniquely a consequence of frustrated absorption. The initial section of the beam was absorbed until the K edge moved to larger energies. For sufficiently high fluences, the opaque transition shifted into the photon energy range of the incoming x rays, effectively forming a transient transparent window in the material. The outcome was an even shorter transmission. At more extreme fluences, the resonant transition shifted into the photon energy range of the incoming x rays but was promptly suppressed by the sheer number of incident photons resulting in a double peak profile with a large FWHM.

We believe the reason for the resonant K – M state’s proliferation and motion along the path of the beam is similar to that of photon energy shifts in emission spectra for high-temperature plasma discussed in literature [12,24,25]. The main mechanism for absorption is K -shell ionization resulting in a single core hole. In copper, fluorescence accounts for 44.5% of the total recombination, while the remaining holes are filled mainly via KLL Auger-Meitner decay [26]. Electron impact is another source of ionization. Hot electrons ejected by collision with the x-ray beam or through Auger-Meitner decay generate further vacancies in the material, triggering an ionization cascade. Primary and secondary ejected electrons equilibrate through collisions with the cold electron reservoir (conduction band). Cold electrons also gain kinetic energy and begin to ionize outer valance states in the material. As more bound electrons exit the atoms, screening of higher levels is reduced and deep states move closer to the nucleus. For high enough charged states the $1s$ – $3p$ transition (most

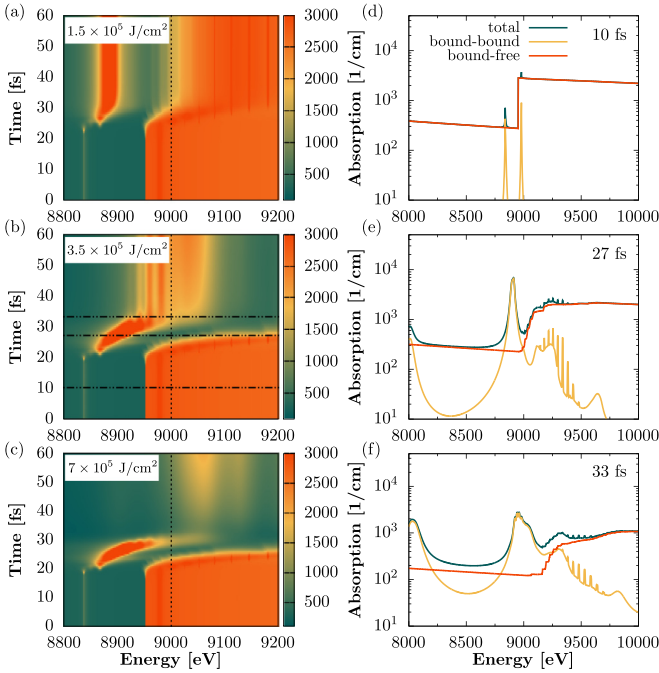


FIG. 5. (a)–(c) Opacity averaged over all zones showing displacement of the K -edge and resonant K – M transition for three incident fluences. The vertical dashed line indicates the XFEL pulse photon energy. Horizontal lines in (b) are cuts through the absorption shown in the three panels to the right. (d)–(f) Opacities at 3.5×10^5 J/cm² averaged over all zones at three instances during the simulation. The 10 fs snapshot shows opacities for a cold sample, the 27 fs shows a dip in the opacity at 9 keV, and the 33 fs snapshot shows an increased opacity at 9 keV.

dominant around 9 keV) increases and shifts into the range of the incident beam. Photoelectrons are no longer ejected to the continuum and are instead resonantly pumped to the M shell [12]. The final transmitted profile duration is determined by the time delay between the K -edge and K – M photon energy changes along the thickness of the sample.

b. Fluorescence profile. For a given fluence we fitted a linear combination of the normalized fluorescence profile given by the simulations using $\hat{I}_F(t) = a_1 \hat{I}_0(t) + a_2 \hat{I}_T(t)$, where a_1 and a_2 are coefficients that changed based on the incident fluence. We found $\hat{I}_F(t)$ at low fluence was mainly described by the transmission profile and at high fluence by the incident profile. More information is found in the Supplemental Material [21]. These changes in the coefficients suggested absorption caused by the K – M resonance extended the temporal duration of the resulting $K\alpha$ emission. We expect fluorescence to follow the incident profile for a linear material response. In a nonlinear regime, the emission’s duration changes at different fluences owing to variations in the opacity. The effects of nonlinearity became apparent at 1.5×10^5 J/cm². Figure 6 shows the result of modifying the photon energy of the incoming x rays. The lowest fluorescence profile FWHM occurred at an incident photon energy of 9.1 keV, where the incident beam completely avoided the resonance. These results indicate the beam’s photon energy could be adjusted to minimize fluorescence duration.

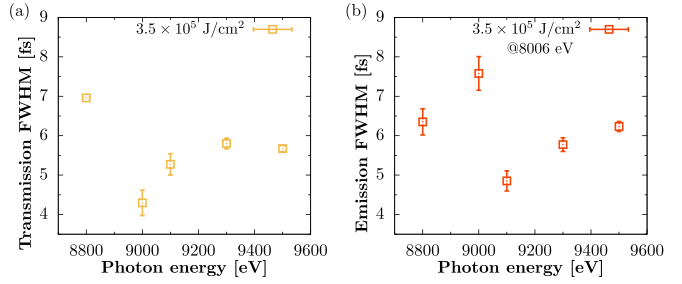


FIG. 6. (a) Transmission and (b) fluorescence durations for an incident beam of varying photon energy and 7 fs FWHM. At 9 keV, fluorescence is prolonged by the resonant K – M transition. The resonance does not extend to 9.1 keV, causing the fluorescence signal to become temporally shorter. See the Supplemental Material [21] for full spectra comparison.

The optical efficiency expected from these two beam reduction techniques is presented for fluences where we expect the most significant pulse reduction. In the case of transmission, we calculated an efficiency of around 0.28–0.46 (based on the number of photons or intensity) for fluences between 2 and 3×10^5 J/cm² at 9 keV photon energy. The efficiency values are comparable with transmittance measured by Inoue *et al.* [8] of around 0.31–0.33. For the fluorescence, we computed an efficiency of 0.0054–0.0077 (based on the number of photons or intensity) with a 3.5×10^5 J/cm² incident beam and 9.1 keV photon energy.

C. Limitations of the model

We are interested in changes to the radiation and copper’s electronic population along the beam’s trajectory. The collisional-radiative code distributes radiation according to the equation of radiative transfer with an assumed infinite speed of light. A 9 keV x-ray beam incident at the front of a cold copper sample then instantly appears along the entire thickness, but with local magnitudes reduced due to absorption by the intervening material. Emission induced by the absorption is one or two orders of magnitude smaller than the incident beam and has a diminished impact on copper’s state. Compared to a model that follows the speed of light, we expect the approximate treatment of the radiation to minimally influence the radiation landscape and state of the material. A graphical description of instant propagation is found in the Supplemental Material [21].

The collisional-radiative code also assumes photoionized electrons instantly thermalize. The energy distribution, which would otherwise be comprised of a thermal and nonthermal contribution [27], remains Maxwellian. As a consequence, the model predicts a greater number of electrons at a higher temperature than the thermal component of a model with a bimodal distribution. Primary ejected electrons cause a cascade of electron impact events that determine electronic, optical, and radiative material changes. For copper, the absolute collision ionization cross section grows with increased electron temperature, peaking at approximately 40–50 eV, and falls slowly at larger temperatures [28]. Highly energetic electrons (>80 eV) are likely to ionize from deep valance shells, while lower-energy electrons ionize from outer valance shells [29].

The average electron temperature in a typical simulation performed in this study can reach several hundreds of eV. For the first few femtoseconds, our simulations could underestimate the secondary ionization of deep valence states, while overestimating outer valence electron ionization. When the electron temperature reaches several hundred eV the simulations could underestimate the outer valence electron ionization. The shift in the resonant state is sensitive to the ionization level of the system [25]. To fully evaluate the effects of electron impact ionization it is necessary to compare results with collisional-radiative codes that evolve the nonthermal electron distribution [30–32].

The screened-hydrogenic atomic model is constructed with data obtained in the isolated atom approximation and requires modifications for application in high-density plasma. The environment shifts the energy levels and changes the ionization balance, captured in our simulations with the Ecker-Kröll (EK) [33] ionization potential depression (IPD) description. Measurement of $K\alpha$ emission in solid aluminum for varying ionization states supports the use of EK [34,35], but He-like and H-like emission on the same material at higher temperatures agrees with a model developed by Stewart and Pyatt (SP) [36,37]. Recent spectroscopy studies on high-pressure copper-doped plastic comparing EK and SP demonstrated disagreement in $K\alpha$ emission and $1s-2p$ absorption features [38]. Fully quantum-mechanical strategies [38–41] more appropriately match experimental aspects of IPD. These advancements have not yet produced simple-enough continuum-lowering models to apply to the nonequilibrium state collisional radiative simulations. In the case of low-temperature XFEL conditions, ionized electrons are less delocalized and contribute more to the screening than assumed in simple theories, which appears to agree more closely with the particular EK version used in collisional-radiative modeling [34,42].

III. CONCLUSIONS AND OUTLOOK

We find that exposure to high-ionizing radiation on a thin copper sample can be used to temporally decrease the duration of an x-ray pulse via transmission and fluorescence. Starting with a 7 fs FWHM beam at 9 keV, we found approximately a 3 fs reduction in transmission. Opacity calculations revealed saturable absorption was partially responsible for the temporal reduction. At sufficiently high intensities shifts in the $K-M$ resonant excitation turned the copper plasma opaque, causing an early transmission termination. The $K-M$ shift also caused extended fluorescence with longer FWHM than the incident beam. By increasing the photon energy we escaped this resonance and achieved as much as a 2 fs reduction in fluorescence at 8006 eV.

We propose the present work can be expanded in three ways.

(1) We hypothesize a two-color scheme, above and below the Cu K edge with femtosecond time delay, can be used to control the transmission profile FWHM and enhance photon yield. The first signal above the edge could trigger a shift in the resonant transition, while the second beam could propagate largely unattenuated until the $K-M$ resonance crosses its path.

(2) An approach to reach shorter profile durations is to use a copper alloy to decrease the time it takes for the resonant

$K-M$ transition to shift to higher energies. For example, nickel has a higher Auger-Meitner yield and can strongly interact with Cu $K\alpha$. A Cu-Ni mixture augments the number of electrons available for electron collision ionization, potentially reaching a high degree of ionization in copper faster.

(3) We can study the effects of modifying the x-ray interaction with matter on saturable absorption by either increasing the beam's photon energy to induce a doubly ionized core (decay channels might be different) or by utilizing nanostructured targets [43]. Controlling x-ray absorption in neon with an optical laser has been reported in the literature [44].

The short pulses predicted in this work or with the above-proposed approaches could be useful for incoherent diffraction imaging of metalloproteins, where the speckle pattern visibility inversely depends on the number of coherent intervals of the fluorescing atoms [45]. Signal reaching the detector from a single exposure with FWHM will contain approximately FWHM/τ_c number of modes, where τ_c is the fluorescence coherence time [7]. A shorter pulse can help preserve contrast in the speckle pattern by reducing the number of modes.

IV. METHODS

We performed one-dimensional nonlocal thermodynamic equilibrium (NLTE) simulations with collisional-radiative code CRETIN v_02_20 [42] and a screened-hydrogenic model (SHM) based on principal quantum numbers. We included solid-density effects via electron degeneracy and continuum lowering to describe a solid to plasma transition. We recorded time-varying radiative properties (opacities and emissivities), material properties (temperature, densities, population states), and detailed radiation spectra. The physical choices presented in this section were made through commands inside the code and their implementation can be found in [42,46]. CRETIN has been compared both with other NLTE codes [47] and with experiments that study warm dense matter originating from the interaction of proteins, water, and metals with soft and hard XFEL beams [48–50].

As a starting configuration, we defined copper as a degenerate and strongly coupled plasma with a fixed density of 8.96 g/cm^3 and temperature of 0.025 eV (290 K); see the Supplemental Material [21] for the time evolution of the plasma state based on the degeneracy and Coulomb parameters. At standard temperature and pressure, solid copper is treated on average as a pseudonoble gas electronic configuration $[\text{Ar}]3d^{10}$ with its $4s$ electron occupying the conduction band. We modeled this band by placing one electron per atom in the continuum. We fixed the plasma starting thermal conductivity to match the copper conductivity at 20°C and 1 bar of $3.86 \times 10^7 \text{ ergs/cm}^2/\text{s}$ [53]. Simulations ran for 60 fs in dynamic steps of ≈ 0.5 fs. Cold opacities are directly calculated from the atomic model.

A. Collisional-radiative algorithm

The collisional-radiative algorithm solves atomic kinetics, radiation transport, density, and temperature equations. For NLTE conditions, the radiation depends on knowledge of the populations, which in turn are modified by the radiation, and the solution is reached self-consistently [54]. The kinetics evaluation uses the extant conditions and radiation field to

establish the material properties, including electron density. Radiation transfer using these properties updates the radiation fields. The atomic kinetics plus radiation transfer supplies heating rates to calculate temperatures. The updated temperatures, densities, and radiation fields influence the kinetics and the loop repeats iteratively until all quantities converge.

a. Atomic kinetics. CRETIN solves atomic kinetics using the rate equation $dy/dt = \mathbf{A} \mathbf{y}$, where \mathbf{A} is the rate matrix and \mathbf{y} is the population of the atomic levels [46]. The rate matrix contains transitions for processes included in the atomic model, which are adjusted based on the density, electron distribution, and incident radiation field. The sample is divided into nodes where atomic kinetics are determined independently based on the local environment [46]. In these simulations, material does not move between nodes and energy exchange is accomplished via radiation transport and thermal conduction [46]. The populations dictate opacities and emissivities, which are passed as inputs to the radiation transfer algorithm.

b. Radiation transfer. CRETIN keeps track of the changing energy landscape with a radiative transfer equation that, for a frequency ν -dependent field I_ν traveling over a straight path s through the sample, is written as $dI_\nu/d\tau_\nu = I_\nu - S_\nu$ [54]. Here $S_\nu \equiv j_\nu/\alpha_\nu$ is the source function defined as the ratio between the emissivity j_ν and extinction coefficient α_ν of the sample and τ_ν is the optical depth along the infinitesimal path ds defined as $d\tau \equiv -\alpha ds$ [54]. The radiative transfer treatment covers the total solid angle by including paths in multiple directions and using the symmetries inherent in the geometry, which for one dimension becomes a “long characteristic” method.

For numerical efficiency, radiation is handled using independent energy spaces with unique grid sizes and ranges. A continuum space is used to evaluate photoionization and photoexcitation integrals that couple to the atomic kinetics and a spectral space is used to construct high-resolution spectra based on real-time plasma conditions [42]. To reduce computational demands on the continuum integrals, we defined a coarse mesh over the photon energy range 0.1 eV–10 keV. We identified optically thick transitions and checked the continuum adequately matched the opacity spectrum. See the Supplemental Material [21] for details. A formal solution to the radiation transfer problem for continuum was obtained using the Feautrier formalism [55]. We considered Stark broadening effects when generating the spectra. To model self-absorption, we used escape factors that interpolate between tabulated values [56] valid for a static material and the Sobolev limit applicable to fast-expanding material. We also included Compton scattering with a $1 + \cos(\theta)^2$ dipole angular dependence.

c. Temperature evolution. The free electrons and ions follow a Maxwellian distribution with temperatures evolved from the coupled differential equations

$$\frac{dT_e}{dt} = \frac{2}{3n_e} \left[R_a + \frac{d}{dx} \left(\kappa_e \frac{dT_e}{dx} \right) \right] - \frac{T_e}{n_e} \frac{dn_e}{dt} + \gamma_{ei}(T_i - T_e) + S_e, \quad (1)$$

$$\frac{dT_i}{dt} = \gamma_{ie}(T_e - T_i) + S_i, \quad (2)$$

where T_e and T_i are the electron and ion temperatures, n_e is the local electron density, R_a is the heating rate from atomic kinetics, κ_e is the electron thermal conductivity, γ_{ei} is the electron-ion coupling, and S_e and S_i are electron and ion source functions for laser absorption and other processes [46]. This formulation focuses on the energy content of the free electron distribution, rather than the total energy content of the plasma. The atomic heating rate includes electron- or photon-induced ionization or recombination, electron collisional excitations or deexcitation, autoionization, electron capture, and bremsstrahlung [46]. We used electron thermal conduction coefficients by Lee and More [57] with a solid-density asymptote, included via a linear conduction term in the temperature equations. Collisions in plasma are mediated by short- and long-distance interactions (hard and soft collisions). The relative cross sections between these two collisional modes are specified by the Coulomb logarithm from Brown and Singleton [58], which also controls bremsstrahlung and laser absorption. We do not include a non-thermal electron distribution. As a consequence, photoejected electrons (folded in the heating rate) instantly thermalize with the continuum.

B. Screened hydrogenic data

A good description of energy levels and transition rates dictates the accuracy of material properties, radiation transport, and spectroscopic features. A problem-specific model based on self-consistent quantum calculations requires a very significant computational effort to construct, particularly if highly ionized and multiply excited states are required, while a general SHM requires much less time to construct and maintains good accuracy for the intended application if inclusive of all configurations involved in the atomic kinetics to produce accurate spectra [59,60]. However, using any single set of screening coefficients produces systematic inaccuracies in level energies which become worse around closed shell ions. A SHM for copper using multiple quantum numbers for all possible ionization states can yield a large number of transitions that quickly becomes incomputable. We limited ourselves to generating data based on principal quantum number (PQN) N following methods described by Scott and Hansen [22] and from a convergence study summarized in the Supplemental Material [21].

We defined $N = 24$ energy levels for each charge state using screening constants from More [61], scaled to match ionization energies from quantum calculations by Liberman *et al.* [62], and allowed a maximum of five possible excitations to the highest N . We also split photoinduced bound-bound transitions between PQNs for up to $N = 6$ for each atomic state and applied an additional width over each transition to represent fine structure details. Scott and Hansen [22] showed the above approach improves the accuracy and distribution of transition energies for xenon resulting in similar spectra compared to that obtained from more sophisticated models.

Rates from photon, electron, and ion collisions are also part of the atomic model. Relevant processes included are (1) photon- or electron-induced ionization and recombination, (2) photon- or electron-induced excitation and deexcitation, and (3) autoionization and electron capture. CRETIN computes

photoinduced transitions and ionizations based on oscillator strengths from screening constants. We used collisional excitation rates from JJATOM [63], collisional ionizations from Golden and Sampson [64], and autoionization from Chung *et al.* [65]. Rates are influenced by the radiation field and free-electron density. Finally, we included ionizations via the collision of slow-moving highly charged ions with neutral atoms using a classical overbarrier charge exchange model [66].

C. Solid density effects

The atomic data used in CRETIN was derived for low density plasmas and is most readily applied with Maxwellian electron distributions to calculate transition rates and material properties. At low temperatures and solid density, electrons instead follow a Fermi-Dirac distribution F_e . Degeneracy effects are included in the code in the following manner. Free electron density and pressure expressions model a degenerate electron gas. Collisional excitation rates are modified with a simple multiplier which closely captures degeneracy effects [67]. Transitions that involve free electrons, such as collisional ionization, require Pauli-blocking factors $P(\epsilon) = 1 - F_e(\epsilon)$ based on electronic occupation [67]. Simple multipliers available for three-body recombination rates are not accurate and can be replaced with numerical integrations. However, the impact of these corrections is usually quite small, so we have used the simpler treatment.

The atomic data is defined for an isolated atom, where we expect the number of energy levels based on PQNs for each charge state to grow large near the ionization boundary [67]. If we now consider the environment, the energy required to ionize a bound electron is lowered by the electrostatic potential of neighboring atoms and free electrons. The existence of Coulomb interactions also modifies the free energy which generally contributes to a negative pressure [67]. Continuum lowering cuts the number of available PQN states and shifts rates, thus altering the opacity and thermodynamics of the system [34]. We employed the Ecker and Kröll [33] continuum lowering model and motivate our choice based on experimen-

tal findings that measured the ionization state of solid-density aluminum from K - α fluorescence emission [34,68]. Ecker and Kröll have been shown to successfully estimate continuum lowering in high-charged states and predict K -edge shifts under conditions similar to those in these experiments [40,69].

The effect of continuum lowering can change dynamically during the simulation. The code gradually reduces each atomic level's statistical weight W using a smooth function. To calculate the lowering weight on each charge state, the code employs the expression

$$W = \exp \left[\frac{\Delta E_{\max} - \Delta E}{\Delta E_{\max}} \right]^\gamma. \quad (3)$$

Here ΔE_{\max} represents the energy that is needed to make the state disappear and ΔE is the degeneracy lowering calculated for the current plasma conditions. The predicted ionization states at various temperatures depends on degeneracy and continuum lowering [70]. The parameter γ was set to 2 and the calculation of ΔE used an ion sphere model that matched copper's conduction band at low temperature and solid density.

ACKNOWLEDGMENTS

The authors would like to thank I. Dawod, C. Vantaraki, Dr. H. P. Le for discussions, and F. Maia for providing the computing resources for simulations. S.C. and N.T. thank the Swedish Research Council (Grant No. 2019-03935) for financial support. C.C. acknowledges the Swedish Research Council (Grant No. 2018-00740) and the Helmholtz Association through the Center for Free-Electron Laser Science at DESY. The work of H.A.S. was performed under the auspices of the U.S. Department of Energy by Lawrence Livermore National Laboratory under Contract No. DE-AC52-07NA27344. H.N.C. and F.T. acknowledge support by the Cluster of Excellence 'Advanced Imaging of Matter' of the Deutsche Forschungsgemeinschaft (DFG)—EXC 2056—project ID 390715994.

-
- [1] A. P. Mancuso, A. Aquila, L. Batchelor, R. J. Bean, J. Bielecki, G. Borchers, K. Doerner, K. Giewekemeyer, R. Graceffa, O. D. Kelsey, Y. Kim, H. J. Kirkwood, A. Legrand, R. Letrun, B. Manning, L. Lopez Morillo, M. Messerschmidt, G. Mills, S. Raabe, N. Reimers *et al.*, *J. Synchrotron Radiat.* **26**, 660 (2019).
 - [2] M. Makita, I. Vartiainen, I. Mohacsi, C. Caleman, A. Diaz, H. O. Jönsson, P. Juranić, N. Medvedev, A. Meents, A. Mozzanica, N. L. Opara, C. Padeste, V. Panneels, V. Saxena, M. Sikorski, S. Song, L. Vera, P. R. Willmott, P. Beaud, C. J. Milne *et al.*, *Sci. Rep.* **9**, 602 (2019).
 - [3] R. W. Lee, S. J. Moon, H.-K. Chung, W. Rozmus, H. A. Baldis, G. Gregori, R. C. Cauble, O. L. Landen, J. S. Wark, A. Ng, S. J. Rose, C. L. Lewis, D. Riley, J.-C. Gauthier, and P. Audebert, *J. Opt. Soc. Am. B* **20**, 770 (2003).
 - [4] R. Neutze, R. Wouts, D. van der Spoel, E. Weckert, and J. Hajdu, *Nature (London)* **406**, 752 (2000).
 - [5] H. N. Chapman, P. Fromme, A. Barty, T. A. White, R. A. Kirian, A. Aquila, M. S. Hunter, J. Schulz, D. P. DePonte, U. Weierstall, R. B. Doak, F. R. N. C. Maia, A. V. Martin, I. Schlichting, L. Lomb, N. Coppola, R. L. Shoeman, S. W. Epp, R. Hartmann, D. Rolles *et al.*, *Nature (London)* **470**, 73 (2011).
 - [6] A. Classen, K. Ayyer, H. N. Chapman, R. Röhlberger, and J. von Zanthier, *Phys. Rev. Lett.* **119**, 053401 (2017).
 - [7] F. Trost, K. Ayyer, and H. N. Chapman, *New J. Phys.* **22**, 083070 (2020).
 - [8] I. Inoue, Y. Inubushi, T. Osaka, J. Yamada, K. Tamasaku, H. Yoneda, and M. Yabashi, *Phys. Rev. Lett.* **127**, 163903 (2021).
 - [9] B. Nagler, U. Zastra, R. R. Faustlin, S. M. Vinko, T. Whitcher, A. J. Nelson, R. Sobierajski, J. Krzywinski, J. Chalupsky, E. Abreu, S. Bajt, T. Bornath, T. Burian, H. Chapman, J. Cihelka, T. Döppner, S. Düsterer, T. Dzelzainis, M. Fajardo, E. Förster *et al.*, *Nat. Phys.* **5**, 693 (2009).

- [10] D. S. Rackstraw, O. Ciricosta, S. M. Vinko, B. Barbrel, T. Burian, J. Chalupský, B. I. Cho, H.-K. Chung, G. L. Dakovski, K. Engelhorn, V. Hájková, P. Heimann, M. Holmes, L. Juha, J. Krzywinski, R. W. Lee, S. Toleikis, J. J. Turner, U. Zastra, and J. S. Wark, *Phys. Rev. Lett.* **114**, 015003 (2015).
- [11] H. Yoneda, Y. Inubushi, M. Yabashi, T. Katayama, T. Ishikawa, H. Ohashi, H. Yumoto, K. Yamauchi, H. Mimura, and H. Kitamura, *Nat. Commun.* **5**, 5080 (2014).
- [12] L. Young, E. P. Kanter, B. Krässig, Y. Li, A. M. March, S. T. Pratt, R. Santra, S. H. Southworth, N. Rohringer, L. F. DiMauro, G. Doumy, C. A. Roedig, N. Berrah, L. Fang, M. Hoener, P. H. Bucksbaum, J. P. Cryan, S. Ghimire, J. M. Glowia, D. A. Reis *et al.*, *Nature (London)* **466**, 56 (2010).
- [13] H. N. Chapman, A. Barty, M. J. Bogan, S. Boutet, M. Frank, S. P. Hau-Riege, S. Marchesini, B. W. Woods, S. Bajt, W. H. Benner, R. A. London, E. Plönjes, M. Kuhlmann, R. Treusch, S. Düsterer, T. Tschentscher, J. R. Schneider, E. Spiller, T. Möller, C. Bostedt *et al.*, *Nat. Phys.* **2**, 839 (2006).
- [14] E. G. Gamaly, *Phys. Rep.* **508**, 91 (2011).
- [15] D. G. Hummer and G. Rybicki, *Annu. Rev. Astron. Astrophys.* **9**, 237 (1971).
- [16] H.-K. Chung and R. Lee, *High Energy Density Phys.* **5**, 1 (2009).
- [17] H.-K. Chung, M. Chen, and R. Lee, *Radiat. Prop. Hot Dense Matter* **3**, 57 (2007).
- [18] M. Rosen, H. Scott, D. Hinkel, E. Williams, D. Callahan, R. Town, L. Divol, P. Michel, W. Kruer, L. Suter, R. London, J. Harte, and G. Zimmerman, *High Energy Density Phys.* **7**, 180 (2011).
- [19] S. P. Hau-Riege, *High-Intensity X-rays-Interaction with Matter: Processes in Plasmas, Clusters, Molecules and Solids* (John Wiley & Sons, New York, 2012).
- [20] A. Madsen, J. Hallmann, G. Ansaldi, T. Roth, W. Lu, C. Kim *et al.*, *J. Synchro. Radi.* **28**, 637 (2021).
- [21] See Supplemental Material at <http://link.aps.org/supplemental/10.1103/PhysRevE.107.015205> for additional details on the optimal fluorescing photon energy, the fluorescence profile model, spectra at two incident photon energies, copper's optical depth, the atomic model convergence and the plasma state over time, which includes Refs. [51,52].
- [22] H. Scott and S. Hansen, *High Energy Density Phys.* **6**, 39 (2010).
- [23] B. I. Cho, M. S. Cho, M. Kim, H.-K. Chung, B. Barbrel, K. Engelhorn, T. Burian, J. Chalupský, O. Ciricosta, G. L. Dakovski, V. Hájková, M. Holmes, L. Juha, J. Krzywinski, R. W. Lee, C. H. Nam, D. S. Rackstraw, S. Toleikis, J. J. Turner, S. M. Vinko *et al.*, *Phys. Rev. Lett.* **119**, 075002 (2017).
- [24] H.-K. Chung, S. B. Hansen, and H. A. Scott, in *Modern Methods in Collisional-Radiative Modeling of Plasmas*, edited by Y. Ralchenko (Springer International Publishing, Cham, 2016), pp. 51–79.
- [25] S. M. Vinko, O. Ciricosta, B. I. Cho, K. Engelhorn, H.-K. Chung, C. R. D. Brown, T. Burian, J. Chalupský, R. W. Falcone, C. Graves, V. Hájková, A. Higginbotham, L. Juha, J. Krzywinski, H. J. Lee, M. Messerschmidt, C. D. Murphy, Y. Ping, A. Scherz, W. Schlotter *et al.*, *Nature (London)* **482**, 59 (2012).
- [26] W. Bambynek, B. Crasemann, R. W. Fink, H. U. Freund, H. Mark, C. D. Swift, R. E. Price, and P. V. Rao, *Rev. Mod. Phys.* **44**, 716 (1972).
- [27] S. P. Hau-Riege, *Phys. Rev. E* **87**, 053102 (2013).
- [28] W. Lotz, *Z. Phys. A: Hadrons Nucl.* **220**, 466 (1969).
- [29] P. L. Bartlett and A. T. Stelbovics, *Phys. Rev. A* **66**, 012707 (2002).
- [30] C. J. Fontes, H. L. Zhang, J. A. Jr, R. E. H. Clark, D. P. Kilcrease, J. Colgan, R. T. Cunningham, P. Hakel, N. H. Magee, and M. E. Sherrill, *J. Phys. B: At., Mol., Opt. Phys.* **48**, 144014 (2015).
- [31] J. J. MacFarlane, I. E. Golovkin, P. R. Woodruff, D. R. Welch, B. V. Oliver, T. A. Mehlhorn, and R. B. Campbell, Simulation of the ionization dynamics of aluminum irradiated by intense short-pulse lasers, in *Proceedings of Inertial Fusion and Science Applications 2003* (American Nuclear Society, La Grange Park IL, 2004), p. 457.
- [32] H. P. Le and J.-L. Cambier, *Phys. Plasmas* **24**, 122105 (2017).
- [33] G. Ecker and W. Kröll, *Phys. Fluids* **6**, 62 (1963).
- [34] O. Ciricosta, S. M. Vinko, H.-K. Chung, B.-I. Cho, C. R. D. Brown, T. Burian, J. Chalupský, K. Engelhorn, R. W. Falcone, C. Graves, V. Hájková, A. Higginbotham, L. Juha, J. Krzywinski, H. J. Lee, M. Messerschmidt, C. D. Murphy, Y. Ping, D. S. Rackstraw, A. Scherz *et al.*, *Phys. Rev. Lett.* **109**, 065002 (2012).
- [35] O. Ciricosta, S. M. Vinko, B. Barbrel, D. S. Rackstraw, T. R. Preston, T. Burian, J. Chalupský, B. I. Cho, H. K. Chung, G. L. Dakovski, K. Engelhorn, V. Hájková, P. Heimann, M. Holmes, L. Juha, J. Krzywinski, R. W. Lee, S. Toleikis, J. J. Turner, U. Zastra *et al.*, *Nat. Commun.* **7**, 11713 (2016).
- [36] D. J. Hoarty, P. Allan, S. F. James, C. R. D. Brown, L. M. R. Hobbs, M. P. Hill, J. W. O. Harris, J. Morton, M. G. Brookes, R. Shepherd, J. Dunn, H. Chen, E. Von Marley, P. Beiersdorfer, H. K. Chung, R. W. Lee, G. Brown, and J. Emig, *Phys. Rev. Lett.* **110**, 265003 (2013).
- [37] J. C. Stewart and K. D. Pyatt, Jr., *Astrophys. J.* **144**, 1203 (1966).
- [38] S. X. Hu, D. T. Bishel, D. A. Chin, P. M. Nilson, V. V. Karasiev, I. E. Golovkin, M. Gu, S. B. Hansen, D. I. Mihaylov, N. R. Shaffer, S. Zhang, and T. Walton, *Nat. Commun.* **13**, 6780 (2022).
- [39] S. Hansen, E. Harding, P. Knapp, M. Gomez, T. Nagayama, and J. Bailey, *High Energy Density Phys.* **24**, 39 (2017).
- [40] S. M. Vinko, O. Ciricosta, and J. S. Wark, *Nat. Commun.* **5**, 3533 (2014).
- [41] S.-K. Son, R. Thiele, Z. Jurek, B. Ziaja, and R. Santra, *Phys. Rev. X* **4**, 031004 (2014).
- [42] H. A. Scott, *Radiat. Prop. Hot Dense Matter* **71**, 689 (2001).
- [43] R. Hollinger, C. Bargsten, V. N. Shlyaptsev, V. Kaymak, A. Pukhov, M. G. Capeluto, S. Wang, A. Rockwood, Y. Wang, A. Townsend, A. Prieto, P. Stockton, A. Curtis, and J. J. Rocca, *Optica* **4**, 1344 (2017).
- [44] T. E. Glover, M. P. Hertlein, S. H. Southworth, T. K. Allison, J. van Tilborg, E. P. Kanter, B. Krässig, H. R. Varma, B. Rude, R. Santra, A. Belkacem, and L. Young, *Nat. Phys.* **6**, 69 (2010).
- [45] J. W. Goodman, *Statistical Optics* (John Wiley & Sons, New York, 2015).
- [46] H. A. Scott and R. W. Mayle, *Appl. Phys. B* **58**, 35 (1994).
- [47] S. Hansen, H.-K. Chung, C. Fontes, Y. Ralchenko, H. Scott, and E. Stambulchik, *High Energy Density Phys.* **35**, 100693 (2020).
- [48] K. R. Beyerlein, H. O. Jönsson, R. Alonso-Mori, A. Aquila, S. Bajt, A. Barty, R. Bean, J. E. Koglin, M. Messerschmidt, D. Ragazzon, D. Sokaras, G. J. Williams, S. Hau-Riege, S. Boutet,

- H. N. Chapman, N. Timneanu, and C. Caleman, *Proc. Natl. Acad. Sci. U.S.A.* **115**, 5652 (2018).
- [49] A. Barty, C. Caleman, A. Aquila, N. Timneanu, L. Lomb, T. A. White, J. Andreasson, D. Arnlund, S. Bajt, T. R. M. Barends, M. Barthelmess, M. J. Bogan, C. Bostedt, J. D. Bozek, R. Coffee, N. Coppola, J. Davidsson, D. P. DePonte, R. B. Doak, T. Ekeberg *et al.*, *Nat. Photon.* **6**, 35 (2012).
- [50] J. Andreasson, B. Iwan, A. Andrejczuk, E. Abreu, M. Bergh, C. Caleman, A. J. Nelson, S. Bajt, J. Chalupsky, H. N. Chapman, R. R. Fäustlin, V. Hajkova, P. A. Heimann, B. Hjärvarsson, L. Juha, D. Klinger, J. Krzywinski, B. Nagler, G. K. Pálsson, W. Singer *et al.*, *Phys. Rev. E* **83**, 016403 (2011).
- [51] S. Rightley and S. D. Baalrud, *Phys. Rev. E* **103**, 063206 (2021).
- [52] D. B. Melrose and A. Mushtaq, *Phys. Rev. E* **82**, 056402 (2010).
- [53] J. Carvill, in *Mechanical Engineer's Data Handbook*, edited by J. Carvill (Butterworth-Heinemann, Oxford, 1993), pp. 102–145.
- [54] M. Carlsson, in *Space Solar Physics*, edited by J. C. Vial, K. Bocchialini, and P. Boumier (Springer, Berlin, Heidelberg, 1998), pp. 163–186.
- [55] P. Feautrier, *C. R. Acad. Sci. Paris* **258**, 3189 (1964).
- [56] J. Apruzese, *J. Quant. Spectrosc. Radiat. Transfer* **34**, 447 (1985).
- [57] Y. T. Lee and R. M. More, *Phys. Fluids* **27**, 1273 (1984).
- [58] L. S. Brown and R. L. Singleton, *Phys. Rev. E* **76**, 066404 (2007).
- [59] J. Rubiano, R. Rodriguez, J. Gil, F. Ruano, P. Martel, and E. Minguez, *J. Quant. Spectrosc. Radiat. Transfer* **72**, 575 (2002).
- [60] S. B. Hansen, in *Modern Methods in Collisional-Radiative Modeling of Plasmas*, edited by Y. Ralchenko (Springer International Publishing, Cham, 2016), pp. 1–15.
- [61] R. M. More, *J. Quant. Spectrosc. Radiat. Transfer* **27**, 345 (1982).
- [62] D. A. Liberman, J. R. Albritton, B. G. Wilson, and W. E. Alley, *Phys. Rev. A* **50**, 171 (1994).
- [63] H.-K. Chung, R. Lee, and M. Chen, *High Energy Density Phys.* **3**, 342 (2007).
- [64] L. B. Golden and D. H. Sampson, *J. Phys. B* **10**, 2229 (1977).
- [65] H.-K. Chung, M. Chen, W. Morgan, Y. Ralchenko, and R. Lee, *High Energy Density Phys.* **1**, 3 (2005).
- [66] F. Sattin, *Phys. Rev. A* **62**, 042711 (2000).
- [67] H. A. Scott, in *Modern Methods in Collisional-Radiative Modeling of Plasmas*, edited by Y. Ralchenko (Springer International Publishing, Cham, 2016), pp. 81–104.
- [68] T. R. Preston, S. M. Vinko, O. Ciricosta, H.-K. Chung, R. W. Lee, and J. S. Wark, *High Energy Density Phys.* **9**, 258 (2013).
- [69] B. Crowley, *High Energy Density Phys.* **13**, 84 (2014).
- [70] A. Ali, G. Shabbir Naz, M. Saleem Shahzad, R. Kouser, Amanur-Rehman, and M. Nasim, *High Energy Density Phys.* **26**, 48 (2018).